Rare Met.
https://doi.org/10.1007/s12598-024-02912-5

RARE METALS

ORIGINAL ARTICLE

Carbon nanofiber catalysts containing high-entropy metal phosphides with low-content Ru for highly efficient hydrogen evolution reaction

Peng Wang, Jie Zheng, Xue-Hao Li, Wen-Bo Cui, Jin-Hua Liu, Yong Wan, Jun Zhang, Yusuke Yamauchi, Zhong-Li Wang, Mang Niu*, Yun-Ze Long*

Received: 25 February 2024 / Revised: 18 April 2024 / Accepted: 2 May 2024

Abstract High-entropy metal phosphide (HEMP) has considerable potential as an electrocatalyst owing to its beneficial properties, including high-entropy alloy synergy as well as the controllable structure and high conductivity of phosphides. Herein, electrospinning and in situ phosphating were employed to prepare three-dimensional (3D) networks of self-supporting HEMP nanofibers with varying degrees of phosphate content. Comprehensive characterizations via X-ray diffraction and X-ray photoelectron spectroscopy, as well as density functional theory calculations, demonstrate that the introduction of phosphorus (P) atoms to HEMP carbon nanofibers mediates their electronic structure, leads to lattice expansion, which in turn enhances their catalytic performance in the hydrogen evolution reaction (HER). Moreover, the formation of metal–P bonds weakens metal–metal interaction and decreases the free energy of hydrogen adsorption, contributing to the exceptional activity observed in the HEMP catalyst. Electrochemical measurements demonstrate that the HEMP-0.75 catalyst with an ultralow loading of 1.22 wt% ruthenium (Ru) exhibits the highest HER catalytic activity and stability in a 1 M KOH electrolyte, achieving a minimal overpotential of 26 mV at a current density of 10 $mA{\cdot}cm^{-2}$ and Tafel slope of 50.9 $mV{\cdot}dec^{-1}$.

Keywords High-entropy metal phosphide; Electrospinning; Hydrogen evolution reaction; Self-supporting carbon nanofibers

Peng Wang and Jie Zheng have contributed equally to this work.

Supplementary Information The online version contains supplementary material available at https://doi.org/10.1007/s12598-024-02912-5.

P. Wang, X.-H. Li, W.-B. Cui, J.-H. Liu, Y. Wan, J. Zhang, Y.-Z. Long*
Shandong Key Laboratory of Medical and Health Textile Materials, College of Physics, Qingdao University, Qingdao 266071, China
e-mail: yunze.long@qdu.edu.cn

J. Zheng
Industrial Research Institute of Nonwovens and Technical Textiles, Shandong Center for Engineered Nonwovens (SCEN), College of Textiles Clothing, Qingdao University, Qingdao 266071, China

J. Zheng, M. Niu*
State Key Laboratory of Bio-Fibers and Eco-textiles, Institute of Biochemical Engineering, College of Materials Science and Engineering, Qingdao University, Qingdao 266071, China
e-mail: mang.niu@qdu.edu.cn

Y. Yamauchi
School of Chemical Engineering and Australian Institute for Bioengineering and Nanotechnology (AIBN), The University of Queensland, Brisbane, QLD 4072, Australia

Y. Yamauchi
Department of Chemical and Biomolecular Engineering, Yonsei University, Seoul 03722, Republic of Korea

Y. Yamauchi
Department of Materials Process Engineering, Graduate School of Engineering, Nagoya University, Nagoya 464-8603, Japan

Z.-L. Wang
Tianjin Key Laboratory of Applied Catalysis Science and Technology, School of Chemical Engineering and Technology, Tianjin University, Tianjin 300072, China

Published online: 22 July 2024

1 Introduction

The development of renewable hydrogen energy is a compelling strategy for addressing the global energy crisis and mitigating environmental pollution resulting from extensive fossil fuel usage [1, 2]. Electrolytic water splitting has emerged as a promising approach for efficient, clean, and sustainable hydrogen production [3–6]; however, the slow kinetics of the hydrogen evolution reaction (HER) necessitates the development of highly active electrocatalysts capable of lowering the reaction energy barrier and enhancing the reaction rate [7–10]. Currently, platinum (Pt)-based catalysts are regarded as the most advanced HER catalysts due to their excellent intrinsic activity; however, their prohibitively high cost and limited availability limit their large-scale deployment [11–13]. The cost of ruthenium (Ru) is only one-third that of Pt. In addition, Ru exhibits a Gibbs free energy of hydrogen adsorption that is considerably close to zero, making it a highly efficient and stable catalytic material for the HER. These advantageous properties make Ru an attractive doping element for high-entropy metal phosphide (HEMP) materials. Consequently, the development of Ru-based catalysts exhibiting high activity, exceptional stability, and cost-effectiveness is considerably beneficial for achieving efficient water decomposition.

Recently, non-Pt-based catalysts, such as transition-metal-based oxides [14], borides [15], nitrides [16, 17], carbides [18] and phosphates [19–23], have been widely studied. Phosphides have specific advantages over other metal compounds as HER catalysts. For example, the P atom has a high electronegativity, allowing it to attract positively charged protons to the active site, thereby increasing the reaction rate of the HER [24–26]. Meanwhile, the higher P-band center of the P atom causes the band gap of P-doped catalysts to be narrow, increasing their conductivity [27, 28]. Overall, the limited active sites and poor stability of transition-metal phosphides in alkaline environments restrict their practical applications.

High-entropy alloys (HEAs) have attracted significant attention in the field of electrocatalysis due to their unique high-entropy properties, such as high-entropy thermodynamic effects, structural lattice distortions, slow diffusion kinetics, and cocktail effects [29–33]. HEAs comprise at least five equimolar or near-equimolar elements mixed in a single solid solution, featuring high-entropy stabilization effects ($\Delta S_{mix} > 1.5R$) [34–36]. As a result of the differences between the electronegativities and atomic sizes of various elements, high-entropy alloy lattices are prone to distortion, which promotes the activation and adsorption of active substances [37, 38]. Furthermore, since the synergistic effect of HEAs can exert a surface ligand effect on corresponding catalysts, the d-band center and electronic structure of the active site can change, improving the catalytic performance of the HER. Kwon et al. [39] prepared ZnNiCoIrX (X = Fe and Mn) HEAs via dealloying. By regulating the electronic structure of the iridium (Ir) active site, the adsorption free energy of intermediates was reduced to achieve excellent catalytic performance. Although much research has been performed on the electrocatalytic performance of HEAs [40], limited research has focused on the regulation of the electronic structure and adsorption free energy of HEA intermediates produced during the synthesis of HEMPs modified via the introduction of P atoms. Many factors, such as conductivity, number of exposed active sites, and electronic structure, influence the HER catalytic performance. Electrospun carbon nanofibers (CNFs) have been shown to exhibit unique advantages as electrocatalyst carriers [41–44]. CNFs possess a high specific surface area and exhibit excellent thermal stability, featuring numerous surficial lattice defects that endow them with inherent electrocatalytic properties. Furthermore, the incorporation of catalytically active components, such as metals and metal phosphides, onto CNFs improves the conductivity of the resulting electrocatalyst while effectively mitigating nanoparticle (NP) aggregation. The active site of the catalyst can be fully exposed through the design of reasonable self-supporting fiber structures (porous or hollow), greatly reducing the amount of catalyst required.

Herein, three-dimensional (3D) networks of self-supported HEMP nanofibers with different degrees of phosphating are prepared by electrospinning and in situ phosphating for the first time. Phytic acid (PA) within the in situ phosphating carbon matrix acts as a phosphorus (P) source and as a chemical crosslinking agent, improving the conductivity of the resulting catalyst. Due to its unique porous structure, the active site of the catalyst is fully exposed, resulting in an excellent HER catalytic activity with a low loading of 1.22 wt% Ru (which is equivalent to 4% of the price of Pt). In addition, the introduction of P atoms to regulate the electronic structure of the HEMP CNFs induces lattice strain while reducing the hydrogen-adsorption free energy, thereby further improving the HER catalytic performance. Electrochemical tests show that the HEMP-0.75 catalyst with a P content of 5.49 wt% exhibits the best HER activity in 1 M KOH, achieving a minimum overpotential of 26 mV to produce a current density of 10 $mA{\cdot}cm^{-2}$ and Tafel slope of 50.9 $mV{\cdot}dec^{-1}$. These values represent a significant improvement over 20 wt% Pt/C (at a current density of 58 $mA{\cdot}cm^{-2}$ and Tafel slope of 79.5 $mV{\cdot}dec^{-1}$). Furthermore, due to the synergistic effects of multiple metals and the introduction of metal–P bonds formed by highly electronegative P atoms, the stability of the catalyst can be increased such that a current density of 12.5 $mA{\cdot}cm^{-2}$ can be obtained with only −

0.058 V verus RHE voltage; this current density can be maintained for > 50 h.

2 Experimental

2.1 Chemicals

Anhydrous ferric trichloride ($FeCl_3$, ≥ 98.0%, Aladdin), cobalt chloride hexahydrate ($CoCl_2{\cdot}6H_2O$, ≥ 98.0%, Aladdin), nickel chloride hexahydrate ($NiCl_2{\cdot}6H_2O$, ≥ 99.9%, Aladdin), manganese chloride tetrahydrate ($MnCl_2{\cdot}4H_2O$, 99.99%, Aladdin), ruthenium chloride trihydrate ($RuCl_3{\cdot}3H_2O$, 95%, Bidepharm), polyacrylonitrile (PAN, M_w = 150,000, Aladdin), poly(styrene) (PS, 98%, Aladdin), N, N-dimethylformamide (DMF, ≥ 99.5%, AR), phytic acid (PA, ≥ 90%, Meryer), potassium hydroxide (KOH, 95%, Aladdin), and nafion solution (5 wt%, Meryer) were used without further purification.

2.2 Materials synthesis

In a typical procedure, 0.25 mmol $FeCl_3$, 0.25 mmol $CoCl_2{\cdot}6H_2O$, 0.25 mmol $NiCl_2{\cdot}6H_2O$, 0.25 mmol $MnCl_2{\cdot}4H_2O$, 0.25 mmol $RuCl_3{\cdot}3H_2O$, 0.94 mmol PA, 0.96 g PAN and 0.4 g PS were dissolved in 11 g DMF. The well-dissolved metal salts/phytic acid/PAN polymer precursor solution was obtained after stirring with a magnetic stirring apparatus for 12 h at 60 °C. Then, the prepared precursor solution was loaded into a plastic syringe with a stainless steel needle and injected into an electrospinning machine with an anode voltage of 20 kV, an injection rate of 0.6 mL·h^{-1}, a distance between the collector and needle of 18 cm, and a rotation speed of 400 r·min^{-1}. The precursor nanofibers were pre-oxidized at 230 °C in the air for 3 h at a heating rate of 2 °C·min^{-1} and then annealed at 1000 °C in an argon atmosphere for 3 h at a heating rate of 2 °C·min^{-1}. Finally, the sample was cooled to room temperature in an argon atmosphere. After carbonization, PS decomposes to create a porous structure in each fiber, resulting in the formation of porous FeCoNiMnRuP HEMP CNFs. The phosphating degree HEMP-x is determined based on the mole ratio of PA:Metal, where PA:Metal = 0:4, 2:4, 3:4, 4:4 are defined as HEMP-0, HEMP-0.5, HEMP-0.75, HEMP-1.0, respectively.

2.3 Materials characterizations

The morphological properties of the samples were observed using a field emission scanning electron microscope (FE-SEM, Regulus 8100, 1 kV) and high-resolution transmission electron microscopy (HRTEM, JEM 2100F, 200 kV). Energy-dispersive X-ray spectroscopy (EDX) mapping images were obtained using scanning transmission electron microscopy (STEM, Sigma 500) at an acceleration voltage of 300 kV. Data from inductively coupled plasma-optical emission spectrometry (ICP-OES) were obtained using the Thermo Fisher iCAP PRO. X-ray diffraction (XRD) investigations were performed on a Smart Lab 3KW diffractometer using Cu Kα (λ = 1.54056 Å). The chemical states of different elements were analyzed via X-ray photoelectron spectroscopy (XPS) using an ESCALAB Xi + X-ray photoelectron spectrometer. The binding energies were calibrated with C 1s (284.8 eV) as the standard. The electrochemical processes were conducted in 1.0 M KOH saturated with Ar and controlled by a CHI760E electrochemical workstation.

2.4 Electrochemical measurements

All electrochemical measurements were performed using a three-electrode system that contained a Hg/HgO reference electrode, a graphite rods counter electrode, and self-supported CNFs-based materials (0.5 cm × 0.5 cm) as the working electrode. All linear sweep voltammetry (LSV) curves were recorded at a scan rate of 5 mV·s^{-1}. The potentials were converted to a reversible hydrogen electrode (RHE) according to the equation $E_{RHE} = E_{Hg/HgO} + 0.098 + 0.059 \times pH$. Pt/C (20 wt%) powder was used as a control and deposited on a glassy carbon electrode (GCE) with a diameter of 5 mm for measurement. The electrocatalyst inks were prepared by dispersing a certain amount of electrocatalysts in a mixed solution of ethanol (49 μL), deionized water (150 μL) and Nafion (9 μL) through a sonication for 30 min. Tafel plots were generated by fitting the linear range of the overpotential (η) and log current densities (lg$j$), using the equation $\eta = b\ \lg(j) + a$, where b is the Tafel slope. The electrochemically active surface area (ECSA) of different samples was determined from cyclic voltammetry (CV) sweeps over a Faraday current-free region at various scan rates. The double layer capacitance (C_{dl}) was calculated using the equation: $C_{dl} = \Delta i/2v$, where v is the scan rate. The ECSA was estimated using the equation: ECSA = C_{dl}/C_s, with a specific capacitance value (C_s) of 0.04 mF·cm^{-2}.

2.5 Computational methods

The density functional theory (DFT) calculations were carried out using Vienna Ab-initio Simulation Package (VASP) [45, 46] with frozen-core all-electron projector-augment-wave (PAW) [47, 48] method. The Perdew–Burke–Ernzerhof (PBE) [49] of generalized gradient approximation (GGA) was adopted to describe the exchange and correlation potential. The cutoff energy for the plane-wave basis set was set to 450 eV. A 5-layer 3 × 3 Fe (111) slab (180 Fe atoms) was used, and a vacuum region of 15 Å above them was used to

ensure the decoupling between neighboring systems. 147 Fe atoms in the Fe (111) slab were randomly replaced by 25 Co, 24 Ni, 90 Ru and 8 Mn atoms to build the model of HEMP-0 ($Fe_4Co_3Ni_3Mn_1Ru_{11}$). The HEMP-0.75 ($Fe_{2.4}Co_{2.35}Ni_{2.31}Mn_{1.95}Ru_{1.22}P_{5.49}$) was simulated by replacing Fe or P atoms in 3-layer 2 × 3 Fe_2PF (111) slab with Co, Ni, Ru and Mn atoms. The geometry optimizations were performed until the forces on each ion were reduced below 0.01 eV·Å^{-1}, and a 1 × 2 × 1 Monkhorst–Pack k-point [50] sampling of the Brillouin zone was used. The DFT-D3 method was used to describe the Van der Waals interaction [51].

The Gibbs free energy (ΔG) is calculated as

$$\Delta G = E_{\mathrm{DFT}} + \Delta E_{\mathrm{ZPE}} - T\Delta S \quad (1)$$

ΔE_{ZPE} is the difference corresponding to the zero point energy between the adsorbed molecule and molecule in the gas phase, and ΔS is one molecule entropy between the absorbed state and gas phase. E_{DFT} is the total energy of the DFT calculated system.

3 Results and discussion

3.1 Synthesis and structural characterization of catalysts

Self-supported FeCoNiMnRuP HEMP CNFs with porous structures were prepared using the electrospinning technique and by subsequent heat treatment (Fig. 1). First, five metal salts, PA, polyacrylonitrile (PAN) and polystyrene (PS) were uniformly dissolved in a dimethylformamide (DMF) solution to prepare a metal salt/PA/PAN/PS precursor solution. Then, this precursor solution was formed into a nanofiber membrane by electrospinning, and the mixed-metal salt and PA were uniformly embedded in the PAN/PS nanofibers (Fig. S1a). In the HEMP–CNF system, PA acts as a P source and as a chemical crosslinking agent to form a supramolecular polymer network through a nucleophilic addition reaction with PAN [52, 53]. During heat treatment, the nanofiber structure is stabilized via pre-oxidation at 230 °C. Subsequently, during carbonization, the FeCoNiMnRu mixed-metal precursors are uniformly dispersed within CNFs, leading to the gradual binding and confinement of metal clusters. At an elevated temperature of 1000 °C maintained for 3 h, the metal atoms acquire sufficient kinetic energy to undergo extensive diffusion, resulting in the uniform formation of single-phase HEA particles [54]. The phosphating mechanism can be described as the P–O bond in the P-containing precursor undergoing cleavage during post-treatment carbonization. This leads to the generation of highly electronegative P species, which are subsequently coordinated with metals, resulting in the formation of metal phosphide nanostructures (HEMP-x). In the HEMP-x CNFs systems, the molar ratio of PA/Metal = x (Table S1) can regulate the degree of phosphating over a wide range. The in situ

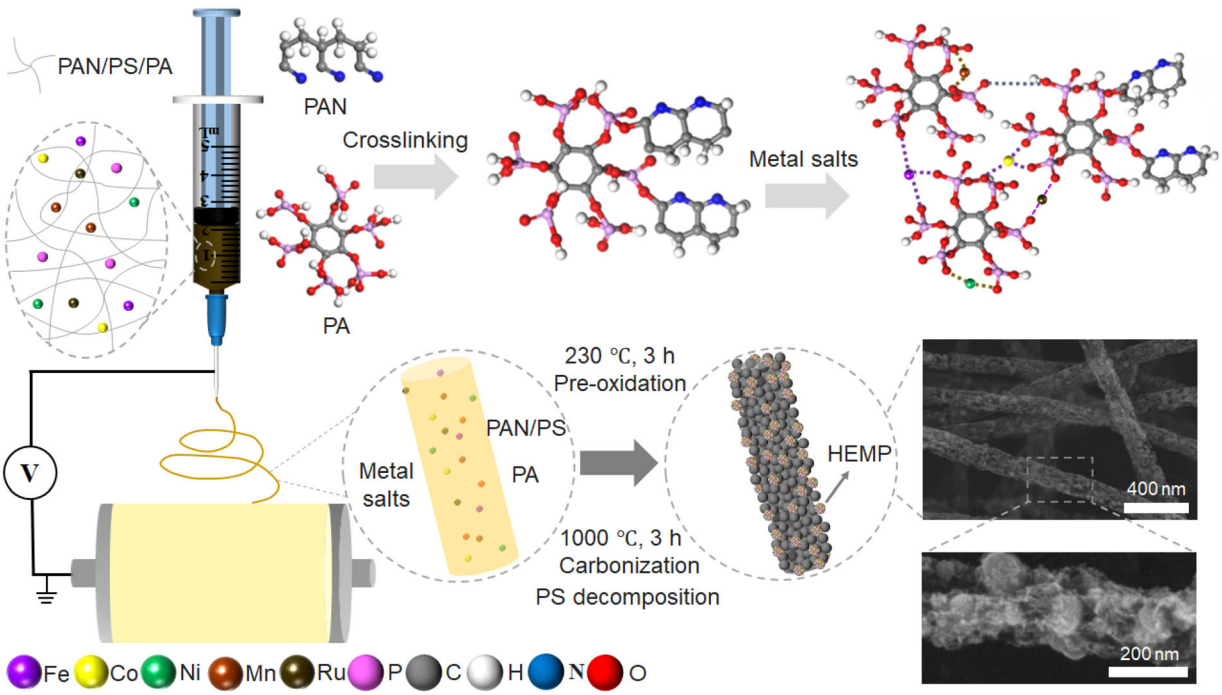

Fig. 1 Schematic diagram of HEMP CNFs with a rich granular porous structure synthesized by electrospinning technology and a subsequent heat treatment process. Possible crosslinking reactions and interactions with metal salts are also presented

phosphating method uses nontoxic, P-containing PA; this eliminates the requirement for toxic P sources while facilitating the in situ formation of a carbon matrix. This carbon matrix reduces the resistance of the resulting catalyst and enhances the overall performance. Furthermore, the presence of six phosphate groups in the PA molecule allows for abundant P atoms to interact strongly with metal ions. These interactions effectively reduce the size of the NPs, leading to improved HER catalytic activity. The precursor solution without PS is electrospun and carbonized to form CNFs with a smooth surface (Fig. S1b). The CNFs added to PS decompose above 800 °C to form porous CNFs (Fig. S1c) [55]. In addition, the formation of HEMP NPs at high temperatures enhances the interaction between PAN molecules near HEMP NPs under the action of PA, leading to the aggregation of HEMP NPs on the fiber surface and in situ phosphorylation, forming a rich granular porous structure of CNFs (Fig. S1d). This structure shows high electrical conductivity and can fully expose the active site of the HEMP NP catalyst. Furthermore, the introduction of P atoms can regulate the electronic structure of the catalyst, allowing HEMP CNFs to exhibit excellent HER performance in the presence of ultralow (1.22 wt%) Ru contents.

The CNFs without HEMP loading were characterized first. Figure S2 shows scanning electron microscopy (SEM) image and scanning transmission electron microscopy–energy-dispersive X-ray (STEM-EDX) mapping image of CNFs, indicating that C, N, O and P are evenly distributed throughout the CNFs. Table S2 shows the contents of C, N, O and P in CNF carriers. XPS was used to determine the chemical states of N and P in CNFs, showing that CNFs primarily contain C–N, P–C and P–O bonds (Fig. S3). Figure 2a shows a FE-SEM image of HEMP-0.75 carbonized at 1000 °C for 3 h, where randomly oriented nanofibers form a typical 3D network structure. Numerous FeCoNiMnRuP NPs, with an average diameter of approximately 35.5 ± 11.2 nm, were densely and uniformly anchored in porous CNFs with an average diameter of approximately 185.5 ± 30.2 nm (Fig. S4). The transmission electron microscopy (TEM) image (Fig. 2b) also shows a uniform distribution of HEMP-0.75 NPs across CNF. High resolution TEM (HRTEM) images show well-resolved lattice fringes with crystal face spacings of 0.221 and 0.203 nm, which can be associated with the (111) and (201) crystal faces of HEMP-0.75 NPs hexagonal phosphide, respectively (Fig. 2c, d) [56]. It is important to note that the lattice spacing of HEMP NPs becomes gradually larger as the degree of phosphating increases (Fig. S5). STEM-EDX elemental mapping images of the HEMP CNFs show that Fe, Co, Ni, Mn, Ru and P are homogeneously distributed throughout each HEMP NP, with no significant elemental separation or phase separation (Fig. 2e). This is due to the high-entropy cocktail effect forming numerous interactions between various elements, promoting a uniform distribution of elements in the lattice and further increasing the complexity of the high-entropy phosphide, thereby enhancing the catalytic activity of HEMP. The concentrations of elements in HEMP-0.75 CNFs were measured by inductively coupled plasma-optical emission spectrometry (ICP-OES). The molar relative percentage of each element in HEMP-0.75 was calculated to be Fe:Co:Ni:Mn:Ru:P = 15:15:15:12:8:35 (Table S3).

The single-phase properties of HEMP were further investigated via XRD. Figure 2f shows XRD patterns of HEMP-0, HEMP-0.5, HEMP-0.75 and HEMP-1.0 with different degrees of phosphorylation. The results show that the introduction of P atoms induced the crystal regulation of the HEAs from the fcc phase (JCPDS No. 47-1417) to the hexagonal phase (JCPDS No. 51-0943) [56]. According to XRD pattern of HEMP-0.75, five diffraction peaks at 2θ = 40.2°, 44.2°, 47.2°, 52.9°, 54.1° and 54.6° were indexed to the (111), (201), (210), (002), (310) and (211) planes of the hexagonal phase. XRD patterns of the HEMP samples mainly show peaks related to the hexagonal phase at appropriate phosphating degrees, and diffraction peaks produced by other phosphates or impurities are not detected; this further demonstrates that no phase separation occurs in HEMP, which is consistent with STEM-EDX results. Interestingly, with increasing P concentration, the peak of the (111) crystal plane of HEMP moves to a lower angle (Fig. 2g). The combination of P, Fe, Co, Ni, Mn and Ru atoms with small atomic sizes increases the atomic-size heterogeneity in the HEAs, leading to the expansion of lattice spacing [57], consistent with observations of HRTEM images. In the case of HEMP-0.75, the P site exhibits moderate electronegativity and a negative charge, effectively functioning as a Lewis base site. This facilitates the trapping of positively charged protons, resulting in a Gibbs free energy of adsorbed hydrogen approaching zero. However, excessive P doping, as in the case of HEMP-1.0, leads to strengthened P–H bonds. Consequently, the adsorption strength of H atoms on the phosphide surface becomes excessively high, ultimately deteriorating the catalytic activity of electrocatalytic hydrogen evolution [58]. These results indicate that CNFs loaded with HEMP NPs are successfully prepared by simple electrospinning and carbonization.

The surface area and pore structure of HEMP CNFs were investigated using N_2 adsorption–desorption isotherms (Fig. 2h). The coexistence of a rough surface with a rich, granular, porous structure and the prevalence of mesopores cause HEMP-0.75 to have a high specific surface area of 468.9 $m^2 \cdot g^{-1}$, which is larger than that of HEMP-0 (327.6 $m^2 \cdot g^{-1}$). This indicates that PA is essential for increasing the size of the active sites. The pore size

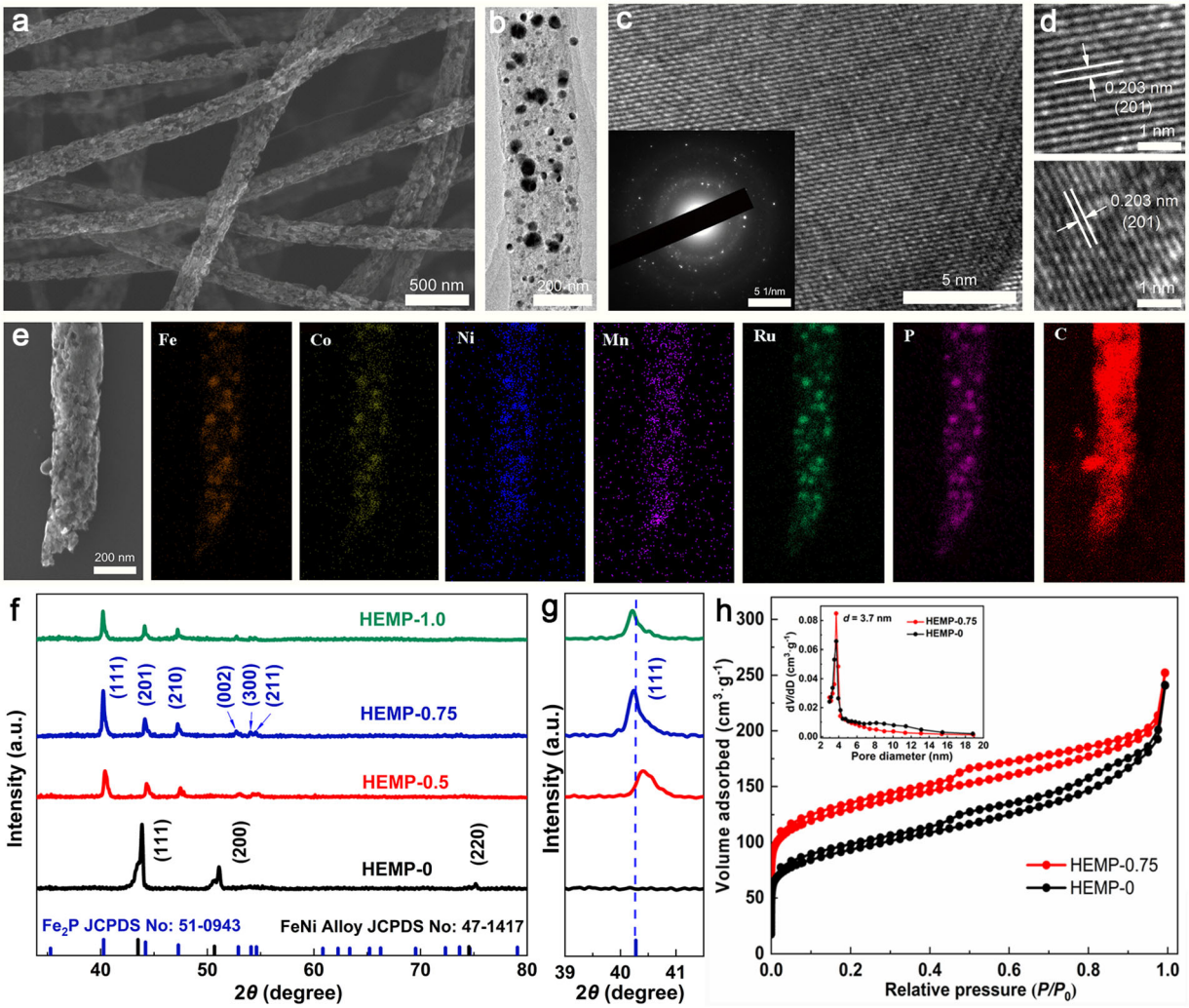

Fig. 2 Morphological and structural characterization of HEMP CNFs. **a** FE-SEM, **b** TEM and **c**, **d** HRTEM images of HEMP-0.75 CNFs; **e** STEM-EDX elemental mapping of HEMP NPs loaded on CNF; **f** XRD patterns of HEMP CNFs with different phosphating degrees; **g** amplified XRD patterns of HEMP CNFs corresponding to **f**; **h** N_2 adsorption–desorption isotherms and pore size distribution curves

distribution plot (Fig. 2h, inset) confirms the microporous and mesoporous properties of HEMP-0.75.

The surface chemical compositions and electronic effects of HEMP CNFs were studied via XPS. Figure S6 shows XPS survey spectrum of HEMP-0 and HEMP-0.75. Notably, the peaks of Fe 2p and Ru 2p in HEMP-0.75 show negative shifts of 0.64 and 0.65 eV, respectively, compared to those of HEMP-0 (Fig. 3a–e). After phosphating, the peaks of Fe 2p, Mn 2p, and Ru 2p shift toward lower binding energies, indicating that electrons are mostly transferred from P to Fe, Mn and Ru atoms, resulting in negative charges on the surface of Fe, Mn and Ru atoms, confirming the change in the electronic structure of the HEA system [59]. In the P 2p high-resolution XPS spectrum of HEMP-0.75 shown in Fig. 3f, the binding energy peaks at 134.2 and 130.1 eV correspond to the P–O and P–metal bonds induced by surface phosphide oxidation, respectively, indicating the formation of P–metal bonds in the HEMP samples [60]. The XPS spectra of Fe, Co, Ni, Mn, Ru and P show that the five metal elements and P coexist in the HEMP CNFs, consistent with the mapping results of STEM, which again confirms the formation of HEMP NPs.

3.2 HER electrocatalytic activities

To evaluate the electrochemical properties of the self-supporting HEMP CNFs, the as-prepared electrocatalysts, Hg/HgO, and graphite rods were used as the working electrodes, reference electrodes and counter electrodes, respectively, of a typical three-electrode system. The HER activities of porous HEMP CNFs with different P contents

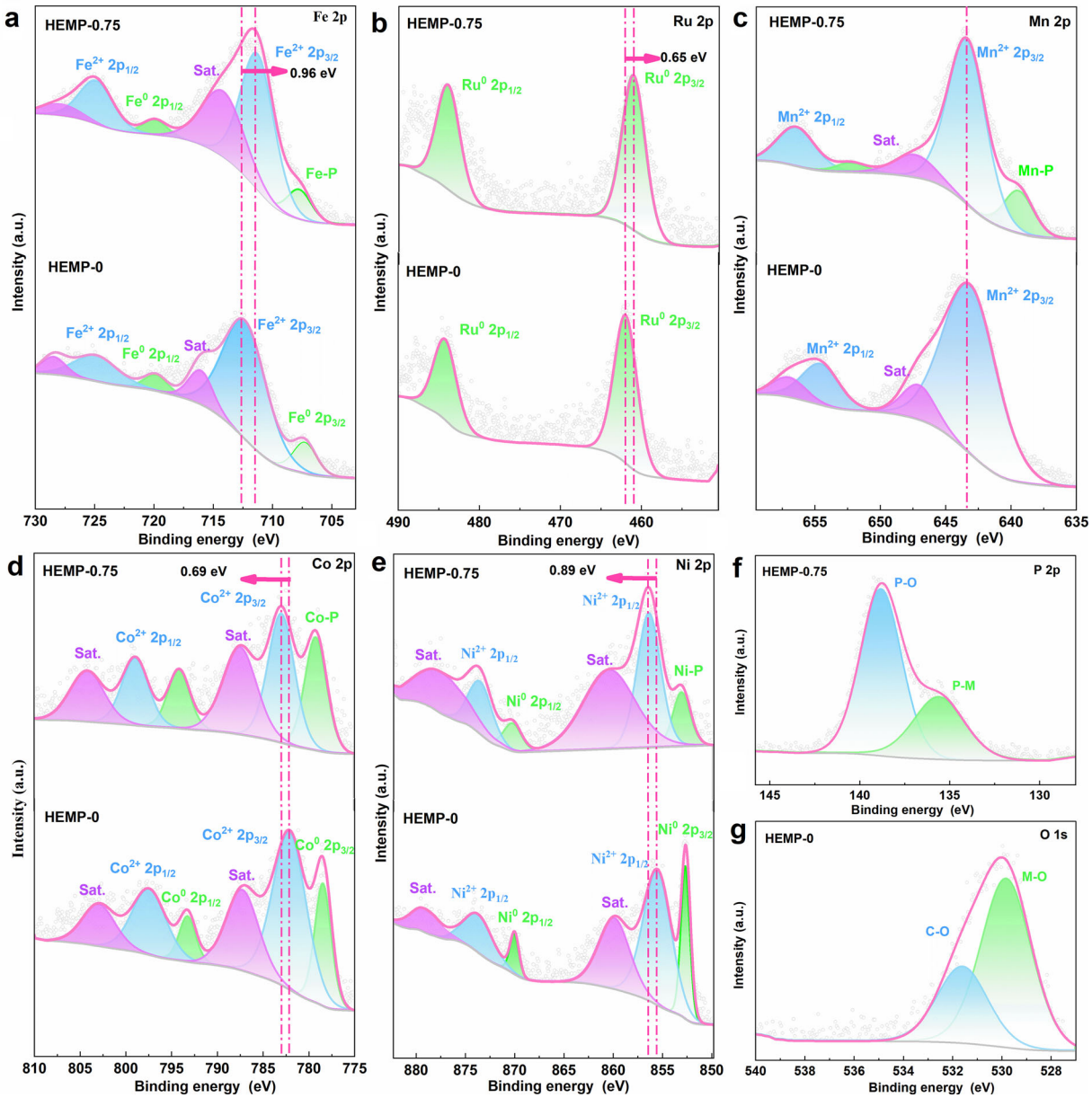

Fig. 3 Surface chemical states of HEMP CNFs investigated via high-resolution XPS. XPS spectra are shown for HEMP-0 and HEMP-0.75: **a** Fe 2p, **b** Ru 2p, **c** Mn 2p, **d** Co 2p and **e** Ni 2p; XPS spectra of **f** P 2p for HEMP-0.75 and **g** O 1s for HEMP-0

were preliminarily detected in a 1 M KOH electrolyte to confirm that the introduction of P atoms can regulate the electronic structure and thus increase catalyst activity. HER LSV curves (Fig. 4a) show that the HEMP CNFs exhibit excellent HER performance. In particular, the HER activity of HEMP-*x* was significantly increased following the introduction of P atoms. HEMP-0.75 was observed to exhibit the best catalytic activity, achieving a minimum overpotential of 26 mV to produce a current density of 10 $mA{\cdot}cm^{-2}$ and a Tafel slope of 50.9 $mV{\cdot}dec^{-1}$ (Fig. 4b). XRD, XPS and DFT calculations indicate that the introduction of P modifies the electronic structure of Ru, thereby promoting the adsorption and desorption of Ru–H, which is crucial for enhancing the HER performance of the HEMP. This catalyst represents a significant improvement over 20 wt% Pt/C (at a current density of 58 $mA{\cdot}cm^{-2}$ and Tafel slope of 79.5 $mV{\cdot}dec^{-1}$); indeed, its performance is better than most previously reported HER electrocatalysts (Table S4). The overpotentials and Tafel slopes of HEMP-*x* catalysts at 10 $mA{\cdot}cm^{-2}$ are shown in Fig. 4c. When the molar ratio of PA/metal increases from 0 to 0.75, the overpotential gradually decreases from 106 to 26 mV and the Tafel slope decreases from 157.1 to 50.9 $mV{\cdot}dec^{-1}$ at a current density of

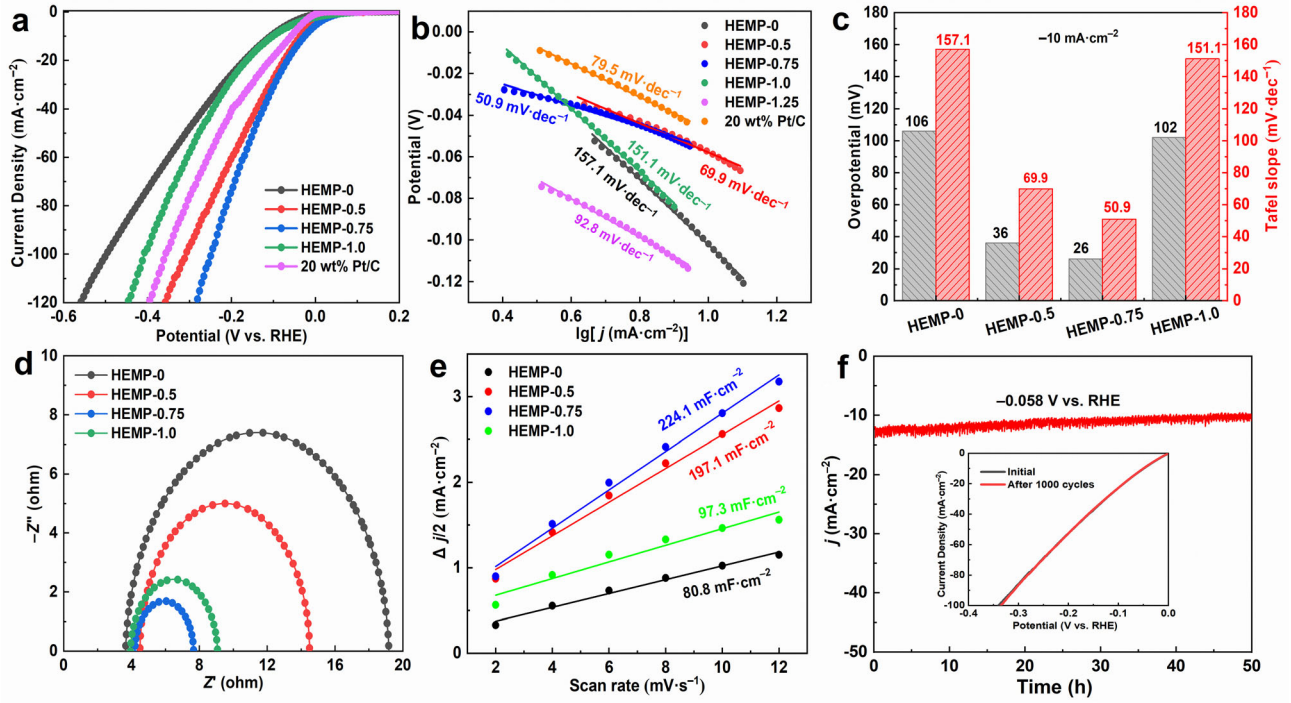

Fig. 4 Electrochemical performance of porous self-supported HEMP CNFs in 1.0 M KOH. **a** HER polarization curves; **b** Tafel slopes of electrocatalysts; **c** histograms of overpotential and Tafel slopes of HEMP CNFs at different phosphating degrees; **d** Nyquist plots; **e** plots of current density versus scan rate for HEMP-0, HEMP-0.5, HEMP-0.75, HEMP-1.0 and HEMP-1.25; **f** long-term stability measurement results of HEMP-0.75 CNFs at − 0.058 V versus RHE in a 1 M KOH electrolyte for 50 h, and (inset) corresponding polarization curves before and after 1000 CV cycles

10 mA·cm^{-2}. In contrast, when excessive P doping is applied, the activity decreases, and the overpotential and Tafel slope increase to 102 mV and 151.1 mV·dec^{-1}, respectively, at 10 mA·cm^{-2} were observed in HEMP-1.0. In general, the overpotential and the Tafel slope of the above catalysts showed the same changing trend. According to the principles of the HER in electrolytic water, HER in the presence of an alkaline electrolyte can be divided into two steps [61, 62]: (1) during the electrochemical reduction of H_2O, an electron is obtained to produce H_{ads} and OH^- (Volmer reaction; Eq. (2)) with a Tafel slope of 118 mV·dec^{-1}; and (2) either H_{ads} with a slope of 39 mV·dec^{-1} reacts with nearby H_2O to produce H_2 and OH^- (Heyrovsky reaction; Eq. (3)) or a neighboring H_{ads} with a slope of 30 mV·dec^{-1} produces H_2 (Tafel reaction; Eq. (4)) [63]. Because HEMP-0 provides a Tafel slope of 157.1 mV·dec^{-1}, the Volmer reaction is the resolution step of the HER, and the kinetics of the H_{ads} adsorption process are slow. As the phosphating degree increases, the Tafel slope value decreases significantly, indicating that the desorption of H_{ads} was promoted due to the weakening of metal-H. HEMP-0.75 exhibits the lowest Tafel slope of 50.9 mV·dec^{-1} at the appropriate phosphating degree. In this case, the Heyrovsky or Tafel reaction process is the controlling step of the HER reaction rate, and the H_{ads} desorption process occurs more rapidly. According to the LSV curve, the introduction of excess P atoms into HEMP-1.0 results in slow kinetics, thereby increasing the Tafel slope. This occurs because the increase of P atoms, due to the negative effect of electronegative P atoms on electron delocalization, causes the conductivity of the catalyst to be reduced, thereby reducing its catalytic performance [64].

$$\text{Volmer}: \quad H_2O + e^- \rightarrow H_{ads} + OH^- \tag{2}$$

$$\text{Heyrovsky}: \quad H_{ads} + H_2O + e^- \rightarrow OH^- + H_2 \tag{3}$$

$$\text{Tafel}: \quad H_{ads} + H_{ads} \rightarrow H_2 \tag{4}$$

Figure 4d shows the Nyquist plots of HER for HEMP-*x* catalysts, where the diameter of the semicircle represents the charge transfer resistance (R_{ct}). The R_{ct} (3.4 Ω) of HEMP-0.75 is much smaller than that of HEMP-0 (15.4 Ω), HEMP-0.5 (9.9 Ω), and HEMP-1.0 (5.2 Ω), indicating that HEMP charge transfer occurs more rapidly when the appropriate phosphating degree, i.e., that most conducive to accelerating the reaction kinetics, is used during the HER process. To further explore the reasons for the high HER activity of HEMP-0.75, CV curves were used to measure the double layer capacitances (C_{dl}) at different scanning rates, and the ECSA of the catalyst was calculated (Fig. S7). As shown in Fig. 4e, the C_{dl} value of HEMP-0.75

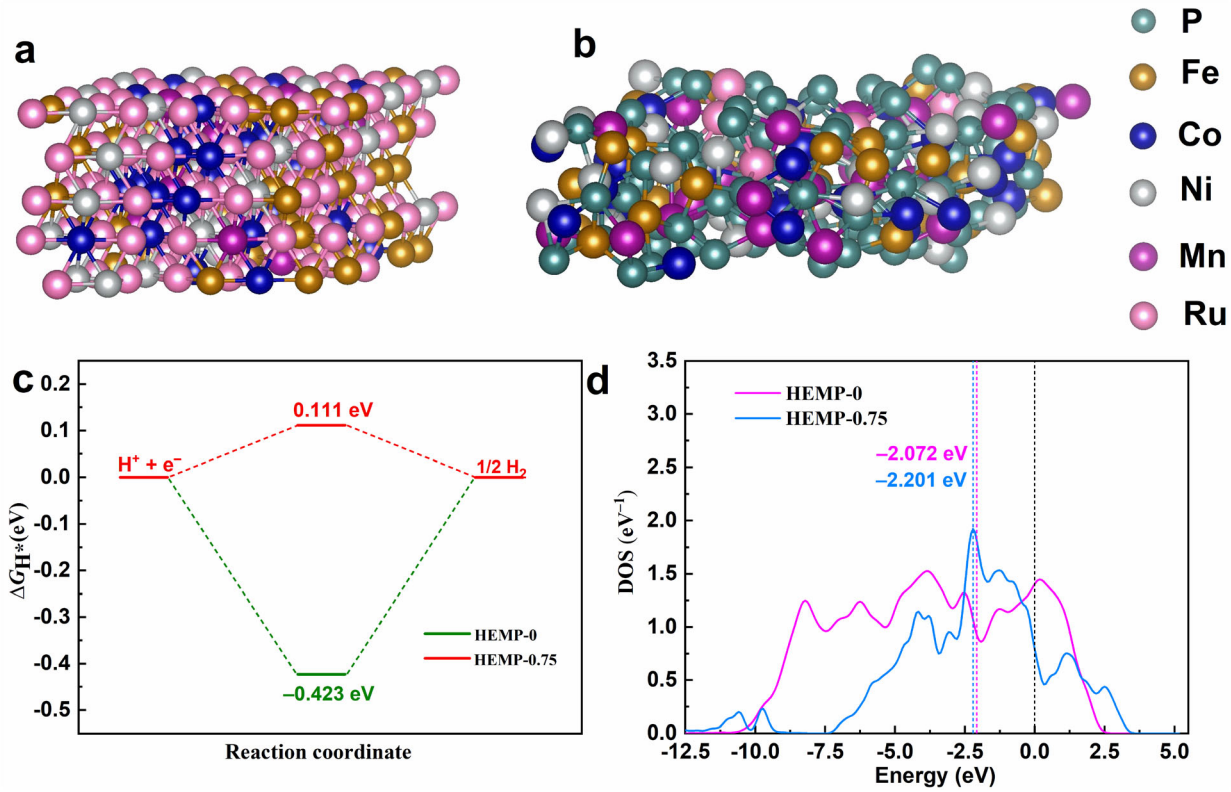

Fig. 5 DFT-calculation-based optimized structures of **a** HEMP-0 and **b** HEMP-0.75; **c** Gibbs free energies of H* adsorption (ΔG_{H^*}) on optimal Ru active sites in HEMP-0 and HEMP-0.75; **d** DOSs of optimal Ru active sites in HEMP-0 and HEMP-0.75. Fermi level is shown as a black dashed line, and d-band centers of optimal Ru active sites in Ru and P-doped Ru alloys are shown as purple and blue dashed lines, respectively

is 224.1 mF·cm^{-2} (ECSA = 5602.5 cm^2). A large ECSA value indicates that more catalytically active sites are exposed on porous CNFs. A small charge transfer resistance and large active surface area can be considered to account for the outstanding catalytic activity observed [54].

The stability of the HEMP-0.75 catalyst was evaluated via repeated LSV and *I–t* tests in a 1 M KOH solution. Figure 4f shows that the HEMP-0.75 catalyst can achieve a current density of 12.5 mA·cm^{-2} with only − 0.058 V versus RHE voltage and can maintain stability for > 50 h. Figure 4f (inset) shows the LSV curve of the catalyst before and after 1000 CV cycles with no obvious deviation. In addition, the HEMP-0.75 catalyst was characterized after the *I–t* test. SEM and STEM-EDX images confirm that the HEMP NPs retain their integrity with no significant morphological degradation after the *I–t* test (Fig. S8). In addition, high-resolution XPS analysis indicates minimal changes in the chemical states of Fe, Co, Ni, Mn and Ru on the surface of the HEMP-0.75 catalyst (Fig. S9). However, a notable reduction in the peak intensity of metal–P bonds is observed, indicating the possible oxidation of the metal–P bonds on the catalyst surface during the stability test. This oxidation is presumed to be the primary factor responsible for the slight decrease in the current density observed for HEMP-0.75 after the stability test.

3.3 First-principles calculations

DFT calculations were performed to investigate H* adsorption and the electronic properties of HEMP-0 ($Fe_{20}Co_{15}Ni_{15}Mn_5Ru_{45}$) and HEMP-0.75 ($Fe_{15}Co_{15}Ni_{15}Mn_{12}Ru_8P_{35}$). Figure 5a shows the optimized structure of HEMP-0, indicating that there are 18 types of surface Ru active sites for H* adsorption. HEMP-0.75, featuring five types of surface Ru active sites, is shown in Fig. 5b. In each case, the top site of surface Ru atoms was used as the H* adsorption site in Gibbs free energy calculations. The optimized structures of HEMP-0 and HEMP-0.75 during H* adsorption are shown in Figs. S10, S11, respectively, and the corresponding Gibbs free energies of H* adsorption (ΔG_{H^*}) are summarized in Table S5, S6. The optimal ΔG_{H^*} values of HEMP-0 and HEMP-0.75 were − 0.432 and 0.111 eV, respectively (Fig. 5c). The catalytic mechanism of HEMP-*x* for the HER involved the occupancy of electrons in the P atom after doping, which takes up a part of the bonding orbital on the

surface of the HEA catalyst. This interaction forms a strong π bond with the metal d orbital, weakening H–metal bonds and facilitating hydrogen desorption [65, 66]. Consequently, HEMP-0.75 shows improved HER performance compared to that of HEMP-0 due to the decreased adsorption ability of H^* on surface Ru active sites. The density of states (DOS) of the optimal active site of Ru 4d in HEMP-0 and HEMP-0.75 is shown in Fig. 5d. The zero energy was set at the Fermi level. The d-band centers of Ru 4d in HEMP-0 and HEMP-0.75 were at − 2.072 and − 2.201 eV, respectively. The fact that the d-band center of the Ru 4d orbital is far from the Fermi level after P doping also proved that Ru doping can weaken the H^* adsorption ability, thereby improving the HER performance. Bader charge analysis indicated that the charges of the optimal active sites of the Ru atom were 8.109 and 8.074 for HEMP-0 and HEMP-0.75, respectively. Consequently, P doping in HEMP-0 led to a charge loss of the optimal Ru active site, causing the d-band center of the Ru 4d orbital to be far from the Fermi level. Furthermore, due to the relatively high H^* adsorption by Ru, the introduction of P atoms shifted the center of the d-band downward, weakening the hydrogen adsorption strength and enhancing the HER performance [67].

4 Conclusion

A HEMP CNF with an adjustable phosphating degree has been prepared by electrospinning technology and in situ phosphating. Its 3D self-supporting fiber network structure can fully expose the active sites required for HER catalysis, thereby increasing the number of active sites available. In addition, the introduction of P atoms can regulate the electronic structure of HEMP CNFs and induce lattice expansion, improving the intrinsic activity of the HER catalyst. Various experiments and DFT calculations have been performed, verifying that P atoms can adjust the lattice structure of HEAs, reduce the free energy of hydrogen adsorption, and exhibit excellent electrochemical properties in catalysts loaded with ultralow Ru contents. Electrochemical tests show that the HEMP-0.75 catalyst in the HEMP-*x* system has the best HER catalytic activity in 1 M KOH and exhibits a low overpotential of 26 mV at a current density of 10 $mA{\cdot}cm^{-2}$. Moreover, the introduction of metal–P bonds formed by highly electronegative P atoms can increase the stability of the catalysts. This research has demonstrated the feasibility of adjusting the electronic structure of HEAs through the simple design of a porous self-supporting nanofiber structure and in situ phosphating. The platform developed can be extended to other group-V metal elements or anions with different valence states, thereby eliciting new possibilities for the preparation of efficient, low-cost and high-activity self-supporting electrocatalysts for industrial hydrogen production.

Acknowledgements This work was financially supported by the National Natural Science Foundation of China (Nos. 22103045 and 52273077) and the State Key Laboratory of Bio-Fibers and Eco-Textiles, Qingdao University (Nos. ZDKT202108, RZ2000003334 and G2RC202022). Yusuke Yamauchi would like to gratefully acknowledge the financial support from the Australian National Fabrication Facility's Queensland Node (No. ANFF-Q), the UQ-Yonsei International Research Project, and the JST-ERATO Yamauchi Materials Space-Tectonics Project (No. JPMJER2003).

Declarations

Conflict of interests The authors declare that they have no conflict of interest.

References

[1] Guo JX, Zheng Y, Hu ZP, Zheng CY, Mao J, Du K, Jaroniec M, Qiao SZ, Ling T. Direct seawater electrolysis by adjusting the local reaction environment of a catalyst. Nat Energy. 2023;8(3):264. https://doi.org/10.1038/s41560-023-01195-x.

[2] Zheng RY, Liu ZC, Wang YD, Xie ZK, He MY. The future of green energy and chemicals: rational design of catalysis routes. Joule. 2022;6(6):1148. https://doi.org/10.1016/j.joule.2022.04.014.

[3] Xie HP, Zhao ZY, Liu T, Wu YF, Lan C, Jiang WCA, Zhu LY, Wang YP, Yang DS, Shao ZP. A membrane-based seawater electrolyser for hydrogen generation. Nature. 2022;612(7941):673. https://doi.org/10.1038/s41586-022-05379-5.

[4] Shah AH, Zhang ZS, Huang ZH, Wang SB, Zhong GY, Wan CZ, Alexandrova AN, Huang Y, Duan XF. The role of alkali metal cations and platinum-surface hydroxyl in the alkaline hydrogen evolution reaction. Nat Catal. 2022;5(10):923. https://doi.org/10.1038/s41929-022-00851-x.

[5] Zhao X, He D, Xia BY, Sun Y, You B. Ambient electrosynthesis toward single-atom sites for electrocatalytic green hydrogen cycling. Adv Mater. 2023;35(14):2210703. https://doi.org/10.1002/adma.202210703.

[6] Cai ZX, Xia YJ, Ito Y, Ohtani M, Sakamoto H, Ito A, Bai YJ, Wang ZL, Yamauchi Y, Fujita T. General synthesis of MOF nanotubes via hydrogen-bonded organic frameworks toward efficient hydrogen evolution electrocatalysts. ACS Nano. 2022;16(12):20851. https://doi.org/10.1021/acsnano.2c08245.

[7] Zhou KL, Wang ZL, Han CB, Ke XX, Wang CH, Jin YH, Zhang QQ, Liu JB, Wang H, Yan H. Platinum single-atom catalyst coupled with transition metal/metal oxide heterostructure for accelerating alkaline hydrogen evolution reaction. Nat Commun. 2021;12(1):3783. https://doi.org/10.1038/s41467-021-24079-8.

[8] Wang LF, Yang RX, Fu JZ, Cao YY, Ding RF, Xu XH. Vertically aligned W(Mo)S_2/N-W(Mo)C-based light-assisted electrocatalysis for hydrogen evolution in acidic solutions. Rare Met. 2023;42(5):1535. https://doi.org/10.1007/s12598-022-02250-4.

[9] Zhao XJ, Chang Y, He XL, Zhang HQ, Jia JC, Jia ML. Understanding ultra-dispersed CeO_x modified iridium clusters as bifunction electrocatalyst for high-efficiency water splitting in acid electrolytes. J Rare Earths. 2023;41(2):208. https://doi.org/10.1016/j.jre.2022.01.013.

[10] Deng X, Zheng XD, Gong ZW, Tan WY, Pei XD. Research progress on single metal atom catalysts for hydrogen production by PEM water electrolysis with lower costs. Chinese Journal of Rare Metals. 2023,47(1):43. https://doi.org/10.13373/j.cnki.cjrm.XY22060014.

[11] Zhang L, Doyle-Davis K, Sun XL. Pt-based electrocatalysts with high atom utilization efficiency: from nanostructures to single atoms. Energy Environ Sci. 2019;12(2):492. https://doi.org/10.1039/c8ee02939c.
[12] Cao YZ, Zheng JN, Wu H, Xu LX, Ye MF, Wan C. Advances in hydrogen production by ammonia borane hydrolysis over Pt-based catalysts. Chin J Rare Met. 2023;47(8):1122. https://doi.org/10.13373/j.cnki.cjrm.XY22060035.
[13] Sun C, Zhao YJ, Yuan XY, Li JB, Jin HB. Bimetal nanoparticles hybridized with carbon nanotube boosting bifunctional oxygen electrocatalytic performance. Rare Met. 2022;41(8):2616. https://doi.org/10.1007/s12598-022-02021-1.
[14] Yang GC, Jiao YQ, Yan HJ, Xie Y, Wu AP, Dong X, Guo DZ, Tian CG, Fu HG. Interfacial engineering of MoO_2-FeP heterojunction for highly efficient hydrogen evolution coupled with biomass electrooxidation. Adv Mater. 2020;32(17):2000455. https://doi.org/10.1002/adma.202000455.
[15] Lee E, Fokwa BPT. Nonprecious metal borides: emerging electrocatalysts for hydrogen production. Acc Chem Res. 2022;55(1):56. https://doi.org/10.1021/acs.accounts.1c00543.
[16] Shi H, Dai TY, Wan WB, Wen Z, Lang XY, Jiang Q. Mo-/Co-N-C hybrid nanosheets oriented on hierarchical nanoporous Cu as versatile electrocatalysts for efficient water splitting. Adv Funct Mater. 2021;31(28):2102285. https://doi.org/10.1002/adfm.202102285.
[17] Li C, Lepre E, Bi M, Antonietti M, Zhu J, Fu Y, Lopez-salas N. oxygen-rich carbon nitrides from an eutectic template strategy stabilize Ni, Fe nanosites for electrocatalytic oxygen evolution. Adv Sci. 2023;10(22):2300526. https://doi.org/10.1002/advs.202300526.
[18] Yu Y, Wang XL, Zhang HK, Cao ZQ, Wu HY, Jia BR, Yang JJ, Qu XH, Qin ML. Facile synthesis of transition metal carbide nanoparticles embedded in mesoporous carbon nanosheets for hydrogen evolution reaction. Rare Met. 2022;41(7):2237. https://doi.org/10.1007/s12598-022-01991-6.
[19] Chen D, Bai HW, Zhu JW, Wu C, Zhao HY, Wu DL, Jiao JX, Ji PX, Mu SC. Multiscale hierarchical structured NiCoP enabling ampere-level water splitting for multi-scenarios green energy-to-hydrogen systems. Adv Energy Mater. 2023;13(22):2300499. https://doi.org/10.1002/aenm.202300499.
[20] Huang LC, Yao RQ, Wang XQ, Sun S, Zhu XX, Liu XH, Kim MG, Lian JS, Liu FZ, Li YQ, Zong HX, Han S, Ding XD. In situ phosphating of Zn-doped bimetallic skeletons as a versatile electrocatalyst for water splitting. Energy Environ Sci. 2022;15(6):2425. https://doi.org/10.1039/d1ee02764f.
[21] Lv S, Deng Y, Liu Q, Fu Z, Liu X, Wang M, Xiao Z, Li B, Wang L. Carbon-quantum-dots-involved Fe/Co/Ni phosphide open nanotubes for high effective seawater electrocatalytic decomposition. Appl Catal B. 2023;326:122403. https://doi.org/10.1016/j.apcatb.2023.122403.
[22] Liu D, Xu GY, Yang H, Wang HT, Xia BY. Rational design of transition metal phosphide-based electrocatalysts for hydrogen evolution. Adv Funct Mater. 2023;33(7):2208358. https://doi.org/10.1002/adfm.202208358.
[23] Wang XY, Le JB, Fei Y, Gao RQ, Jing MX, Yuan WY, Li CM. Self-assembled ultrasmall mixed Co-W phosphide nanoparticles on pristine graphene with remarkable synergistic effects as highly efficient electrocatalysts for hydrogen evolution. J Mater Chem A. 2022;10(14):7694. https://doi.org/10.1039/d2ta00555g.
[24] Du M, Li D, Liu S, Yan J. Transition metal phosphides: a wonder catalyst for electrocatalytic hydrogen production. Chin Chem Lett. 2023;34(9):108156. https://doi.org/10.1016/j.cclet.2023.108156.
[25] Zhang H, Li HY, Zhou YT, Tan F, Dai RJ, Liu XJ, Hu GZ, Jiang LM, Chen AR, Wu RB. Heterostructured bimetallic phosphide nanowire arrays with lattice- torsion interfaces for efficient overall water splitting. J Energy Chem. 2023;77:420. https://doi.org/10.1016/j.jechem.2022.10.019.
[26] Wang XY, Fei Y, Chen J, Pan YX, Yuan WY, Zhang LY, Guo CX, Li CM. Directionally in situ self-assembled, high-density, macropore-oriented, CoP-impregnated, 3D hierarchical porous carbon sheet nanostructure for superior electrocatalysis in the hydrogen evolution reaction. Small. 2022;18(2):2103866. https://doi.org/10.1002/smll.202103866.
[27] Zhang A, Liang YX, Zhang H, Geng ZG, Zeng J. Doping regulation in transition metal compounds for electrocatalysis. Chem Soc Rev. 2021;50(17):9817. https://doi.org/10.1039/d1cs00330e.
[28] Wu L, Su FH, Liu T, Liu GQ, Li Y, Ma T, Wang YF, Zhang C, Yang Y, Yu SH. Phosphorus-doped single-crystalline quaternary sulfide nanobelts enable efficient visible-light photocatalytic hydrogen evolution. J Am Chem Soc. 2022;144(45):20620. https://doi.org/10.1021/jacs.2c07313.
[29] Yao YG, Dong Q, Brozena A, Luo J, Miao JW, Chi MF, Wang C, Kevrekidis IG, Ren ZJ, Greeley J, Wang GF, Abraham A, Hu LB. High-entropy nanoparticles: Synthesis-structure-property relationships and data-driven discovery. Science. 2022;376(6589):151. https://doi.org/10.1126/science.abn3103.
[30] Li HD, Lai JP, Li ZJ, Wang L. Multi-sites electrocatalysis in high-entropy alloys. Adv Funct Mater. 2021;31(47):2106715. https://doi.org/10.1002/adfm.202106715.
[31] Wei M, Sun Y, Ai F, Xi S, Zhang J, Wang J. Stretchable high-entropy alloy nanoflowers enable enhanced alkaline hydrogen evolution catalysis. Appl Catal B. 2023;334:122814. https://doi.org/10.1016/j.apcatb.2023.122814.
[32] Wang Y, Luo W, Gong S, Luo L, Li Y, Zhao Y, Li Z. Synthesis of high-entropy alloy nanoparticles by step-alloying strategy as superior multifunctional electrocatalyst. Adv Mater. 2023;35(36):2302499. https://doi.org/10.1002/adma.202302499.
[33] Pacchioni G. High-entropy materials go nano. Nat Rev Mater. 2022;7(3):156. https://doi.org/10.1038/s41578-022-00429-w.
[34] Tao L, Sun MZ, Zhou Y, Luo MC, Lv F, Li MG, Zhang QH, Gu L, Huang BL, Guo SJ. A general synthetic method for high-entropy alloy subnanometer ribbons. J Am Chem Soc. 2022;144(23):10582. https://doi.org/10.1021/jacs.2c03544.
[35] Zeng KZ, Zhang JW, Gao WQ, Wu LP, Liu HW, Gao JL, Li ZZ, Zhou JH, Li T, Liang ZQ, Xu BJ, Yao YG. Surface-secorated high-entropy alloy catalysts with significantly boosted activity and stability. Adv Funct Mater. 2022;32(33):2204643. https://doi.org/10.1002/adfm.202204643.
[36] Cai ZX, Bolar S, Ito Y, Fujita T. Enhancing oxygen evolution reactions in nanoporous high-entropy catalysts using boron and phosphorus additives. Nanoscale. 2024;16(9):4803. https://doi.org/10.1039/d3nr06065a.
[37] Lin L, Ding ZM, Karkera G, Diemant T, Kante MV, Agrawal D, Hahn H, Aghassi-Hagmann J, Fichtner M, Breitung B, Schweidler S. High-entropy sulfides as highly effective catalysts for the oxygen evolution reaction. Small Struct. 2023;4(9):2300012. https://doi.org/10.1002/sstr.202300012.
[38] Cai ZX, Goou H, Ito Y, Tokunaga T, Miyauchi M, Abe H, Fujita T. Nanoporous ultra-high-entropy alloys containing fourteen elements for water splitting electrocatalysis. Chem Sci. 2021;12(34):11306. https://doi.org/10.1039/d1sc01981c.
[39] Kwon J, Sun S, Choi S, Lee K, Jo S, Park K, Kim YK, Park HB, Park HY, Jang JH, Han H, Paik U, Song T. Tailored electronic structure of Ir in high entropy alloy for highly active and durable bifunctional electrocatalyst for water splitting under an acidic environment. Adv Mater. 2023;36(26):2300091. https://doi.org/10.1002/adma.202300091.
[40] Wang Y, Gong N, Liu HF, Ma W, Hippalgaonkar K, Liu Z, Huang YZ. Ordering-dependent hydrogen evolution and oxygen

reduction electrocatalysis of high-entropy intermetallic Pt_4FeCoCuNi. Adv Mater. 2023;35(28):2302067. https://doi.org/10.1002/adma.202302067.
[41] Zhang FZ, Chen J, Wallace GG, Yang JP. Engineering electrocatalytic fiber architectures. Prog Mater Sci. 2023;133:101069. https://doi.org/10.1016/j.pmatsci.2023.101069.
[42] Zhu H, Sun SH, Hao JC, Zhuang ZC, Zhang SG, Wang TD, Kang Q, Lu SL, Wang XF, Lai FL, et al. A high-entropy atomic environment converts inactive to active sites for electrocatalysis. Energy Environ Sci. 2023;16(2):619. https://doi.org/10.1039/d2ee03185j.
[43] Hu Q, Wang ZY, Huang XW, Qin YJ, Yang HP, Ren XZ, Zhang QL, Liu JH, He CX. A unique space confined strategy to construct defective metal oxides within porous nanofibers for electrocatalysis. Energy Environ Sci. 2020;13(12):5097. https://doi.org/10.1039/d0ee02815k.
[44] Han Y, Duan H, Liu W, Zhou C, Wang B, Jiang Q, Feng S, Yan W, Tan T, Zhang R. Engineering the electronic structure of platinum single-atom sites via tailored porous carbon nanofibers for large-scale hydrogen production. Appl Catal B. 2023;335:122898. https://doi.org/10.1016/j.apcatb.2023.122898.
[45] Kresse G, Hafner J. Ab-initio molecular-dynamics simulation of the liquid-metal–amorphous-semiconductor transition in germanium. Phys Rev B. 1994;49(20):14251. https://doi.org/10.1103/PhysRevB.49.14251.
[46] Kresse G, Furthmuller J. Efficient iterative schemes for ab initio total-energy calculations using a plane-wave basis set. Phys Rev B. 1996;54(16):11169. https://doi.org/10.1103/PhysRevB.54.11169.
[47] Blochl PE. Projector augmented-wave method. Phys Rev B. 1994;50(24):17953. https://doi.org/10.1103/PhysRevB.50.17953.
[48] Kresse G, Joubert D. From ultrasoft pseudopotentials to the projector augmented-wave method. Phys Rev B. 1999;59(3):1758. https://doi.org/10.1103/PhysRevB.59.1758.
[49] Hammer B, Hansen LB, Norskov JK. Improved adsorption energetics within density-functional theory using revised Perdew–Burke–Ernzerhof functionals. Phys Rev B. 1999;59(11):7413. https://doi.org/10.1103/PhysRevB.59.7413.
[50] Froyen S. Brillouin-zone integration by Fourier quadrature: special points for superlattice and supercell calculations. Phys Rev B. 1989;39(5):3168. https://doi.org/10.1103/PhysRevB.39.3168.
[51] Grimme S, Antony J, Ehrlich S, Krieg H. A consistent and accurate ab initio parametrization of density functional dispersion correction (DFT-D) for the 94 elements H-Pu. J Chem Phys. 2010;132(15):154104. https://doi.org/10.1063/1.3382344.
[52] Gong YX, Xu LH, Li JJ, Shan D. Confinement of transition metal phosphides in N, P-doped electrospun carbon fibers for enhanced electrocatalytic hydrogen evolution. J Alloys Compd. 2021;875:159934. https://doi.org/10.1016/j.jallcom.2021.159934.
[53] Shi ZP, Nie KQ, Shao ZJ, Gao BX, Lin HL, Zhang HB, Liu BL, Wang YX, Zhang YH, Sun XH, Cao XM, Hu P, Gao QS, Tang Y. Phosphorus-Mo_2C@carbon nanowires toward efficient electrochemical hydrogen evolution: composition, structural and electronic regulation. Energy Environ Sci. 2017;10(5):1262. https://doi.org/10.1039/c7ee00388a.
[54] Hao JC, Zhuang ZC, Cao KC, Gao GH, Wang C, Lai FL, Lu SL, Ma PM, Dong WF, Liu TX, Du ML, Zhu H. Unraveling the electronegativity-dominated intermediate adsorption on high-entropy alloy electrocatalysts. Nat Commun. 2022;13(1):2662. https://doi.org/10.1038/s41467-022-30379-4.
[55] Sun J, Zeng L, Jiang HR, Chao CYH, Zhao TS. Formation of electrodes by self-assembling porous carbon fibers into bundles for vanadium redox flow batteries. J Power Sources. 2018;405:106. https://doi.org/10.1016/j.jpowsour.2018.10.035.
[56] Lai DW, Kang QL, Gao F, Lu QY. High-entropy effect of a metal phosphide on enhanced overall water splitting performance. J Mater Chem A. 2021;9(33):17913. https://doi.org/10.1039/d1ta04755h.
[57] Chen Q, Han X, Xu Z, Chen Q, Wu Q, Zheng T, Wang P, Wang Z, Wang J, Li H, Xia Z, Hao J. Atomic phosphorus induces tunable lattice strain in high entropy alloys and boosts alkaline water splitting. Nano Energy. 2023;110:108380. https://doi.org/10.1016/j.nanoen.2023.108380.
[58] Cai JY, Song Y, Zang YP, Niu SW, Wu YS, Xie YF, Zheng XS, Liu Y, Lin Y, Liu XJ, Wang GM, Qian YT. N-induced lattice contraction generally boosts the hydrogen evolution catalysis of P-rich metal phosphides. Sci Adv. 2020;6(1):8113. https://doi.org/10.1126/sciadv.aaw8113.
[59] Huang Y, Jiang LW, Shi BY, Ryan KM, Wang JJ. Highly efficient oxygen evolution reaction enabled by phosphorus doping of the Fe electronic structure in iron-nickel selenide nanosheets. Adv Sci. 2021;8(18):2101775. https://doi.org/10.1002/advs.202101775.
[60] Li A, Zhang L, Wang F, Zhang L, Li L, Chen H, Wei Z. Rational design of porous Ni–Co–Fe ternary metal phosphides nanobricks as bifunctional electrocatalysts for efficient overall water splitting. Appl Catal B. 2022;310:121353. https://doi.org/10.1016/j.apcatb.2022.121353.
[61] Huang CL, Lin YG, Chiang CL, Peng CK, Senthil Raja D, Hsieh CT, Chen YA, Chang SQ, Yeh YX, Lu SY. Atomic scale synergistic interactions lead to breakthrough catalysts for electrocatalytic water splitting. Appl Catal B. 2023;320:122016. https://doi.org/10.1016/j.apcatb.2022.122016.
[62] Yu ZY, Duan Y, Feng XY, Yu XX, Gao MR, Yu SH. Clean and affordable hydrogen fuel from alkaline water splitting: past, recent progress, and future prospects. Adv Mater. 2021;33(31):2007100. https://doi.org/10.1002/adma.202007100.
[63] Li Z, Li B, Yu M, Yu C, Shen P. Amorphous metallic ultrathin nanostructures: a latent ultra-high-density atomic-level catalyst for electrochemical energy conversion. Int J Hydrog Energy. 2022;47(63):26956. https://doi.org/10.1016/j.ijhydene.2022.06.049.
[64] Yu WL, Gao YX, Chen Z, Zhao Y, Wu ZX, Wang L. Strategies on improving the electrocatalytic hydrogen evolution performances of metal phosphides. Chin J Catal. 2021;42(11):1876. https://doi.org/10.1016/s1872-2067(21)63855-x.
[65] Zhou SZ, Jang H, Qin Q, Hou LQ, Kim MG, Liu SG, Liu XE, Cho J. Boosting hydrogen evolution reaction by phase engineering and phosphorus doping on Ru/P-TiO_2. Angew Chem Int Ed. 2022;61(47):e202212196. https://doi.org/10.1002/anie.202212196.
[66] Guo K, Fan DP, Bao JC, Li YF, Xu DD. Atomic-level phosphorus-doped ultrathin Pt nanodendrites as efficient electrocatalysts. Adv Funct Mater. 2022;32(47):2208057. https://doi.org/10.1002/adfm.202208057.
[67] Yang JH, Yang SX, An LL, Zhu J, Xiao JW, Zhao X, Wang DL. Strain-engineered Ru-NiCr LDH nanosheets boosting alkaline hydrogen evolution reaction. ACS Catal. 2024;14(5):3466. https://doi.org/10.1021/acscatal.3c05550.